RESEARCH ARTICLE
doi: 10.2306/scienceasia1513-1874.2026.021

ScienceAsia 52 (1): 2026: ID 2026021: **1–7**

FeS_2@SnO_2 composite as a high-performance anode material for lithium-ion batteries

Zekun Tu, Lijie Cao*

Shanghai University of Engineering Science, Songjiang, Shanghai, China

*Corresponding author, e-mail: 2905441071@qq.com

Received 26 Sep 2025, Accepted 17 Feb 2026
Available online 22 Mar 2026

ABSTRACT: In this study, FeS_2 nanoparticles prepared by hydrothermal synthesis were ultrasonically dispersed in the SnO_2 precursor solution. After undergoing 6-h aging at ambient conditions (25 ± 2 °C), the mixture was dried and dehydrated to prepare FeS_2@SnO_2 composite designed for high-capacity lithium-ion battery anodes. The results reveal that the prepared FeS_2@SnO_2 composite consists of flaky FeS_2 nanoparticles exhibiting a size distribution of 100–600 nm, and SnO_2 nanocrystals filled the gaps between and covered the FeS_2 nanoparticle substrate. The electrochemical test results indicate that the prepared FeS_2@SnO_2 composite demonstrates a superior initial capacity (843.7 mAh/g) and enhanced cycling stability compared to FeS_2 anodes. The excellent electrochemical characteristic of the FeS_2@SnO_2 composite may be attributed to the introduction of SnO_2, which adjusts the original electronic structure of FeS_2, improves lithium ion transport efficiency, and effectively inhibits the structural collapse of FeS_2 at the cost of some active reaction sites, thereby endowing the FeS_2@SnO_2 composite with better structural stability.

KEYWORDS: lithium-ion batteries, FeS_2, anode material, composite material, electrochemical performance

INTRODUCTION

With the rapid development of the automotive industry, the new-generation automotive industry has garnered significant attention for lithium-ion batteries (LIBs) as energy storage devices in automotive applications in recent years. To address the increasing commercial need for energy storage systems, the development of lithium-ion batteries with higher energy density has become the current research focus. Anode material mainly plays the role of adsorption and storage of lithium ions in LIBs, and the choice of anode materials will have a direct influence on the power density and cycling stability of LIBs [1, 2]. Transition metal compounds have great potential as anode materials [3]. Among these options, FeS_2 has received considerable focus due to its large specific capacity (894 mAh/g, $FeS_2 + 4e^- + 4Li^+ \longleftrightarrow Fe + 2Li_2S$) and high lithium-ion diffusion efficiency, it is expected to replace graphite-based materials and become the negative electrode material of advanced LIBs with superior energy density [3, 4]. Xu et al [5] reported that the FeS_2@rGO material, coated with rGO, achieves a primary discharge capability of 1640.9 mAh/g with an applied current density of 100 mA/g and can maintain a specific capacity reaching over 800 mAh/g at high 1 A/g current density. Liu et al [6] stated that they synthesized hollow, egg yolk-shell-structured, flower-like nanospheres, which retained a capacity of 709.9 mAh/g after 200 charge-discharge cycles with an applied current density of 200 mA/g. Zhang et al [7] reported that bud-shaped FeS_2 microspheres have initial specific charge-discharge capacities of 773 mAh/g and 749 mAh/g. He et al [8] reported a rapid nonhydrogel synthesis method, the resulting FeS_2@CNT composite material exhibited a high specific capacity approaching 1200 mAh/g after 100 charge-discharge cycles at 100 mA/g.

Although the predicted specific capacity of FeS_2 is relatively large, its conductivity and ion transport efficiency are relatively low, which can lead to severe polarization phenomena, and the volume undergoes significant changes during the charge/discharge cycling [9, 10]. This leads to structural degradation of the material, which in turn affects the cycle stability and lifespan of LIBs. By introducing other organic or inorganic materials to construct composite structures with FeS_2, the structural stability and capacity retention of FeS_2 can be significantly improved. Among various inorganic materials, SnO_2 has excellent chemical stability and a suitable lithiation potential (about 1.0 V vs. Li/Li^+), and as a LIB anode material, it demonstrates a theoretical capacity reaching 1494 mAh/g. SnO_2 can regulate its original crystal structure and electrical conductivity without changing its lattice constant by forming doped composite structures with other metal elements. Moreover, the construction of composite structures helps to adjust the lithiation potential of the negative electrode material, making it more compatible with the working voltage range of FeS_2 materials, thereby constructing an ion-optimized architecture for enhanced Li^+ diffusion and further enhancing the overall electrochemical performance and safety of LIBs. For instance, Cheng et al [11] reported a ternary composite nanoparticle composed of SnO_2-MoO_2-GO (SMGO), which significantly enhanced electrical conductivity through rational structural design that shortened electron transport pathways. This ternary com-

posite nanoparticle retained a high specific capacity of 1032.9 mAh/g after 1000 charge-discharge cycles at a current density of 1.0 A/g. Li et al [12] demonstrated core-shell heterojunction nanofibers composed of SnO_2 and TiO_2, delivering a reversible capacity of 650 mAh/g at a current density of 0.2 A/g with an initial coulombic efficiency of 58.2%. Even at a higher current density of 2 A/g, the LIB retained a reversible capacity of 303 mAh/g after 2000 cycles. Wang et al [13] reported a coating structure that attaches SnO_2 crystal particles onto the surface of nanocarbon spheres. Although the initial discharge capacity decreased to 555 mAh/g, it demonstrated a high capacity retention of up to 87.5% in subsequent cycle tests.

In this work, a $Sn(OH)_4$ suspension was employed as the precursor solution to fabricate the FeS_2@SnO_2 composite-encapsulated structure for application as a LIB anode. The incorporation of SnO_2 modified the original electronic structure of FeS_2, thereby enhancing its electrical conductivity [13, 14]. Compared with the incorporation of organic materials, SnO_2, as a metal compound, is capable of forming a more stable chemical structure with FeS_2 due to the presence of ionic bonding [15]. This structural stability efficiently alleviates the expansion and degradation resulting from continuous lithium-ion intercalation and de-intercalation, thereby enhancing the battery's cycling performance [16]. Furthermore, the introduction of SnO_2 enables the regulation of the lithiation potential of the FeS_2 anode, optimizes the charge-discharge voltage profile, and facilitates more efficient lithium-ion diffusion kinetics, ultimately contributing to the enhanced electrochemical performance and overall stability of the battery system.

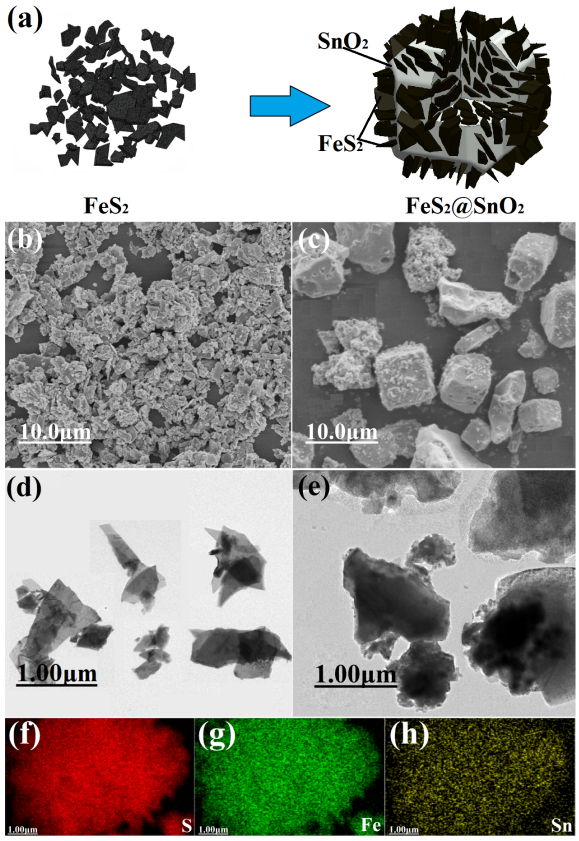

Fig. 1 (a) Illustration of the synthesis process for FeS_2@SnO_2; (b,c) SEM images of FeS_2, FeS_2@SnO_2, (d,e) TEM images of FeS_2@SnO_2; (f–h) elemental maps of FeS_2@SnO_2.

MATERIALS AND METHODS

Materials

All chemical reagents utilized in the experimental process were used as received without further purification. Anhydrous ferrous chloride ($FeCl_2$, analytical reagent (AR), 98%), L-cysteine ($C_3H_7NO_2S$, 98%), sodium hydroxide (NaOH, 97%) and Crystalline tin tetrachloride ($SnCl_4 \cdot 5\,H_2O$, 99%) were obtained from Aladdin Biochemical Technology Co., Ltd., Shanghai, China.

Synthesis of FeS_2

0.38 g of $FeCl_2$ (3 mmol) was added into 60 ml of the prepared 0.15 mol/l L-cysteine solution and stirred with ultrasonic waves for 1 h. The solution was transferred into a 100 ml Teflon-lined high-pressure reactor, heated to 200 °C in a muffle furnace, and maintained at that temperature for 24 h. After permitting the solution to reach ambient temperature upon cooling, the black product from the reaction was collected by centrifugation. The black material was rinsed with ethanol and water at least three times and then dried at 80 °C for 12 h, resulting in the successful preparation of FeS_2 nanoparticles.

Synthesis of FeS_2@SnO_2

0.35 g of $SnCl_4 \cdot 5\,H_2O$ (the molar ratio to FeS_2 is approximately 1 to 3) was added into 100 ml of ethanol, followed by a few drops of NaOH solution (about 1 to 2 ml) and FeS_2 nanoparticles obtained above, followed by ultrasonication for a duration of 4.5 h. The solution was allowed to stabilize at room temperature for 6 h; the reaction products were collected and subsequently washed at least three times with a mixture of ethanol and water. It was then dried at 80 °C for 24 h, ultimately yielding FeS_2@SnO_2.

RESULTS AND DISCUSSION

Material characterization

Fig. 1a illustrates the synthesis process of FeS_2@SnO_2. First, the SnO_2 precursor solution was obtained through the reaction of crystalline $SnCl_4 \cdot H_2O$ with ethanol, and then SnO_2 was deposited onto the surface of the FeS_2 nanoparticles by ultrasonic treatment. An

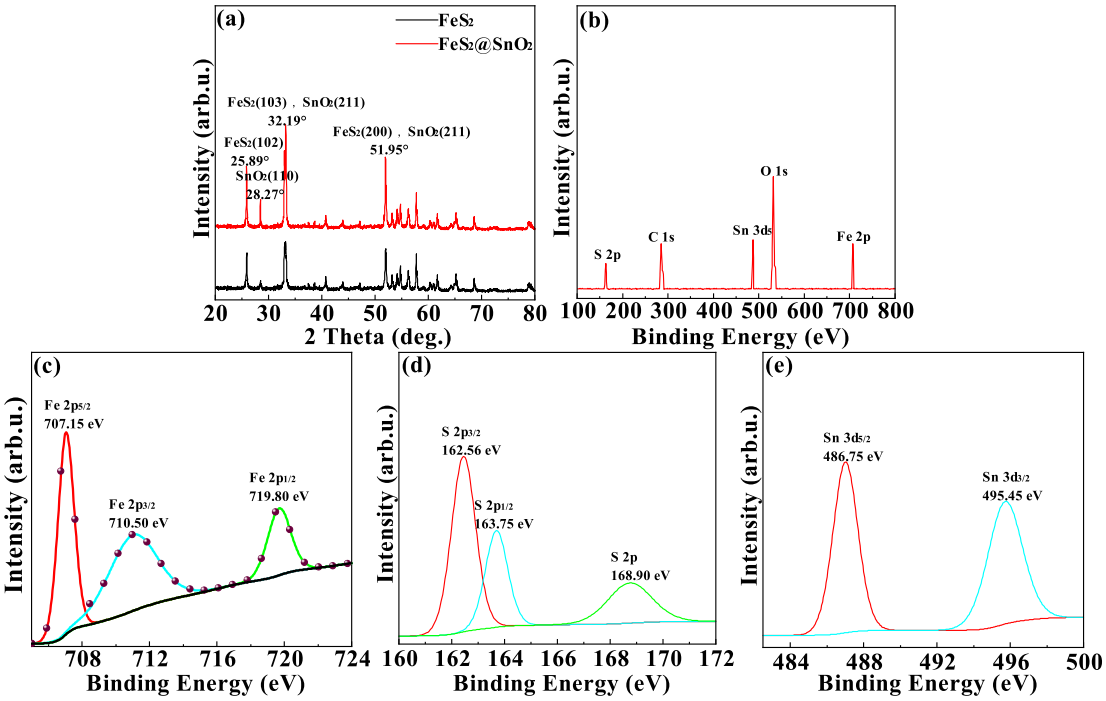

Fig. 2 XRD pattern and XPS spectra of the FeS_2@SnO_2 anode. (a) The XRD pattern of FeS_2@SnO_2; (b) The XPS survey spectrum of FeS_2@SnO_2; (c–e) XPS Fe2p, Sn3d, S2p spectrum.

insufficient content of SnO_2 may lead to difficulties in forming a stable coating structure, whereas an excessive amount can impede the effective contact between FeS_2 and the electrolyte, thereby adversely affecting its electrochemical performance. Therefore, the molar ratio of SnO_2 to FeS_2 should be maintained within the range of 1:3 to 1:4. Fig. 1b shows the SEM image of FeS_2 nanoparticles synthesized hydrothermally. Numerous FeS_2 particles, with diameters ranging from approximately 100 to 600 nm, are observed to aggregate into larger secondary structures. Based on the overall irregular flake-like morphology and disordered arrangement of the nanoparticles, the FeS_2 material in this study is identified as the siderite phase, exhibiting a structurally disordered microstructure. Fig. 1c presents the SEM image of FeS_2@SnO_2, indicating that the FeS_2 nanoparticles in a discrete state aggregate into quasi-square particles with diameters ranging approximately from 1 to 2 µm, which provides further evidence of the successful aggregation and encapsulation of FeS_2 by the addition of SnO_2. From the TEM images of FeS_2 in Fig. 1d and FeS_2@SnO_2 in Fig. 1e, it is evident that with the incorporation of SnO_2, the FeS_2 nanoparticles coalesce into a more regular and uniform structure. Additionally, a 150-nm-thick tin dioxide layer forms on the surface of the aggregated particles. Due to FeS_2 existing in an amorphous state within the composite, only a lattice spacing of d = 0.19 nm can be measured corresponding to the SnO_2 material. Fig. 1f–j illustrates the elemental mapping of FeS_2@SnO_2. Elemental distribution analysis reveals that sulfur (S) and iron (Fe) elements are uniformly distributed throughout the material, while tin (Sn) elements are dispersed in particulate form both within the internal structure and on the surface. This observation provides further confirmation of the formation of the encapsulation structure.

X-ray diffraction (XRD) is extensively employed as a reliable methodology for characterizing and analyzing the crystalline structures of composite materials. In this work, the XRD diffraction patterns of FeS_2 and FeS_2@SnO_2 were comparatively analyzed, as illustrated in Fig. 2a. The FeS_2@SnO_2 composite exhibited distinct diffraction peaks at 25.89°, 28.27°, 32.19°, and 51.95°. Specifically, the peak at 25.89° corresponds to the standard diffraction peak of FeS_2 on the (111) crystal plane. Meanwhile, the diffraction peaks observed at 28.27°, 32.19°, and 51.95° correspond to the (110) and (211) lattice planes of SnO_2, indicating the presence of a rutile or cassiterite crystalline phase of SnO_2. These peaks are commonly associated with tetragonal SnO_2 structures. Additionally, the presence of peaks matching the (100) and (101) crystallographic planes of SnS_2 suggests the possible formation of secondary phases during the synthesis process, potentially due to partial sulfidation of SnO_2 under reaction conditions. Furthermore, two low-intensity peaks were observed within the range of 35° to 45°, with no other sharp

peaks present. This observation suggests that the SnO_2 component within the composite material exhibits a low degree of crystallinity or an amorphous structure. The absence of well-defined diffraction peaks in this region indicates limited long-range atomic order, which may be attributed to the thinness of the SnO_2 layer, its non-uniform deposition, or the presence of structural defects introduced during the encapsulation process.

To achieve a more in-depth insight into the elemental content and chemical characteristics of FeS_2@SnO_2 composites, X-ray photoelectron spectroscopy (XPS) was used to analyze the material's composition and electronic states. As shown in Fig. 2b, the composite material is composed of four elements: Fe, S, Sn, and O. The binding energies of the four elements align with the characteristic ionic bond energies associated with FeS_2 and SnO_2 structures. Fig. 2c–e respectively display the three-dimensional spectra of Fe, S, and Sn. The peaks detected at 707.15 eV and 710.5 eV in Fig. 2c are mainly attributed to the Fe 2p3/2 and Fe 2p5/2 components of FeS_2. The peaks located approximately at 707.15 eV and 710.5 eV indicate the unique chemical state of Fe in FeS_2. This suggests that the majority of Fe ions bond with S ions to form Fe—S bonds, which are essential for maintaining the stability of FeS_2 [17]. In Fig. 2d, three distinct peaks of S 2p at 162.56 eV, 163.75 eV, 169.00 eV can be seen, which were assigned to ionic and covalent bonding of Fe to S, respectively. This enables the composite material to interact and react with ions in the electrolyte, thereby significantly enhancing the material's theoretical capacity. In Fig. 2e, the characteristic peaks at 486.75 eV and 495.45 eV are assigned to the Sn 3d5/2 and Sn 3d3/2 doublet of Sn^{4+} in SnO_2, confirming the presence of a tin oxide framework within the composite. This structural framework enhances both the material's structural stability and surface reactivity, while significantly improving its resistance to electrolyte-induced degradation during electrochemical cycling. Such robust stability constitutes a key factor enabling efficient and durable charge storage and release. Furthermore, no additional secondary peaks attributable to Sn—S or Sn—Fe bonding are observed within the detection limit and spectral resolution of the XPS measurement, suggesting the absence of strong interfacial chemical bonding between SnO_2 and FeS_2, or that any such interactions produce spectroscopic signatures too weak to be resolved under the current experimental conditions [18].

Electrochemical measurements

Considering the unique nanostructures of the FeS_2@SnO_2 composite, its performance as an anode material was comprehensively studied. To further investigate the composite, the electrochemical properties of the FeS_2@SnO_2 hybrid were tested in CR2025 coin-type cells.

After uniformly mixing the active material, conductive agent, and the binder in a mass ratio of 7:3:1, NMP (N-methylpyrrolidone) is gradually added and ground for 30 min. The slurry is uniformly coated onto the copper foil surface, achieving a film thickness of approximately 15 μm and an active mass loading of about 2 mg. The coated electrode is then transferred to a vacuum drying oven and dried at 110 °C for 8 h to yield the experimental electrode. The experimental negative electrode sheet was placed into the shell and secured. An appropriate amount of electrolyte (1 mol/l lithium hexafluorophosphate solution) was then applied to the surface of the negative electrode, followed by the placement of the separator and the lithium foil. Subsequently, foam nickel and a gasket were positioned on top of the lithium foil to serve as a buffer layer. Finally, additional electrolyte was added to ensure complete wetting of the battery components. The shell is closed and sealed with a packaging machine. After standing for 12 h, electrochemical tests can be conducted.

Table 1 The diffusion coefficients of lithium-ion and impedance parameters for different electrodes.

Sample	R_s (Ω)	R_{ct} (Ω)	Σ (Ω cm^{2}s$^{-0.5}$)	D_{Li^+} (cm^2/s)
FeS_2	5.615	108.9	69.078	5.815×10^{-18}
FeS_2@SnO_2	4.66	58.86	57.801	8.304×10^{-18}

Three electrochemical cyclic voltammetry cycles were conducted within a potential window from 0.01 V to 3.0 V at a scanning speed of 0.1 mV/s, and the findings are presented in Fig. 3a. Within the 0–3 V window, characteristic anodic peaks at 1.9 V and 2.5 V were attributed to FeS_2 and SnO_2 oxidation with Li^+, respectively. During the next two cycles, due to the formation of the solid electrolyte interface (SEI), the oxidation peak gradually weakened and stabilized. Furthermore, a pronounced reduction peak was observed near 1.75 V in the initial scan, which can be attributed to the alloying reaction between Fe^{2+}, Sn^{4+}, and Li^+ ions [19]. However, the intensity of this reduction peak significantly diminished in subsequent cycles. A novel reduction peak emerged around 2.0 V, likely due to the formation of SnS2, and became increasingly stable and consistent across subsequent cycles. The discharge/charge curve for FeS_2@SnO_2 is presented in Fig. 3b.

During the initial cycle, the FeS_2@SnO_2 electrode demonstrated a remarkable first-cycle discharge capacity of 843.7 mAh/g and a charge capacity of 610.3 mAh/g, exhibiting 72.3% initial coulombic efficiency. However, the specific capacity decreased in subsequent cycles, primarily due to the formation of a SEI layer on the electrode surface, containing components like Li_2S. The electrode retained 487.8 mAh/g after 100 cycles, demonstrating 85.3% capacity retention and exceptional structural stability. Furthermore, the charge-discharge efficiency stabilized to over 98% after

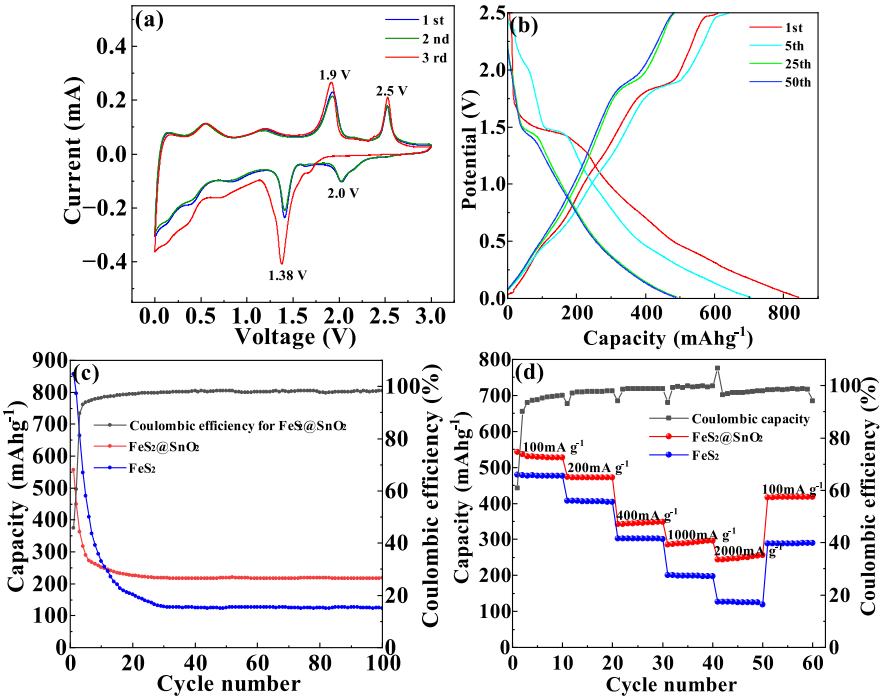

Fig. 3 (a) CV profiles of FeS_2@SnO_2. (b) Discharge/charge curves of FeS_2@SnO_2 at 100 mA/g. (c) Cycling performances and coulombic efficiencies of FeS_2@SnO_2 and FeS_2 at 100 mA/g. (d) Specific capacity and coulombic efficiency of FeS_2@SnO_2 and FeS_2 at 100 mA/g, 200 mA/g, 400 mA/g, 1000 mA/g, and 2000 mA/g.

only 20 cycles, suggesting that the material exhibits excellent energy utilization and capacity retention during repeated charge-discharge processes. These results show that the FeS_2@SnO_2 composite exhibits excellent cycling performance and capacity retention in LIBs, indicating its potential as a high-performance anode material. The charge storage mechanism proceeds via these reaction [13, 20]:

$$FeS_2 + 4e^- + 4Li^+ \longleftrightarrow Fe + 2Li_2S \quad (1)$$

$$SnO_2 + 4e^- + 4Li^+ \longrightarrow Sn + 2Li_2O \quad (2)$$

$$Sn + 4 \cdot 4e^- + 4 \cdot 4Li^+ \longrightarrow Li_{4.4}Sn \quad (3)$$

$$SnS_2 + 4e^- + 4Li^+ \longrightarrow 2Li_2S + Sn \quad (4)$$

To conduct a more comprehensive evaluation of the FeS_2@SnO_2 composites, a comparative analysis was performed with FeS_2 materials. The samples underwent ten charge-discharge cycles under different current density conditions, including 100 mA/g, 200 mA/g, 400 mA/g, 1.0 A/g and 2.0 A/g. Subsequently, the current density was reset to 100 mA/g to evaluate the materials' capacity retention and rate capability. As depicted in Fig. 3d, the FeS_2@SnO_2 composites exhibit average reversible specific capacities of approximately 536.9, 472.0, 346.2, 293.4, and 252.1 mAh/g under five different current density conditions. In contrast, the FeS_2 materials exhibit corresponding specific capacities of approximately 476.7, 405.8, 301.9, 197.9, and 125.5 mAh/g. FeS_2@SnO_2 and FeS_2 anodes showed a significant decrease in specific capacity when tested under high-current testing at 2 A/g. Under high-current charge and discharge conditions, the electrochemical reaction kinetics of the material significantly affect its specific capacity. Due to limited diffusion pathways within the electrode material during high currents, Li^+ ions cannot be completely intercalated [21]. Therefore, these ions tend to remain on the anode material's surface, promoting SEI film formation and ultimately reducing the material's specific capacity [22].

This aggregation-encapsulation structure is established through the clustered arrangement of FeS_2 nanoparticles and the formation of a SnO_2 encapsulation coating on both the surface and internal voids of the clustered structure. The doped SnO_2 layer stabilizes the loose particle structure of FeS_2, resulting in enhanced cycling stability while reducing a portion of the reactive sites. In conclusion, this anode material exhibits exceptional electrochemical properties in LIBs [23].

The EIS technique was employed to comprehensively investigate the electrochemical properties of the FeS_2@SnO_2 electrode under standard environmental conditions. By constructing the equivalent circuit model as shown in the Fig. 4a, the solution resistance and charge transfer resistance of the LIB used in the

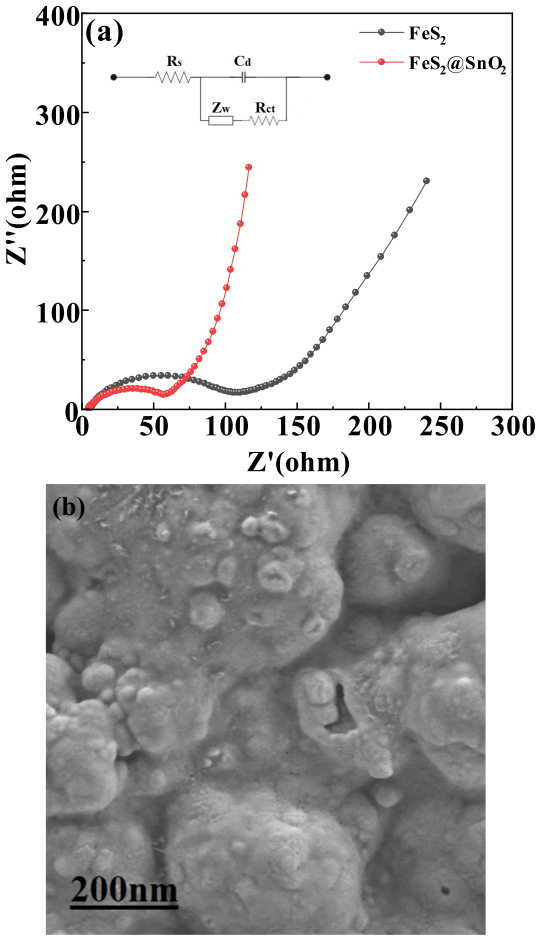

Fig. 4 (a) EIS and equivalent circuit diagrams of FeS_2@SnO_2 and FeS_2 anodes. (b) FeS_2@SnO_2 nanosphere electrode after 100 cycles.

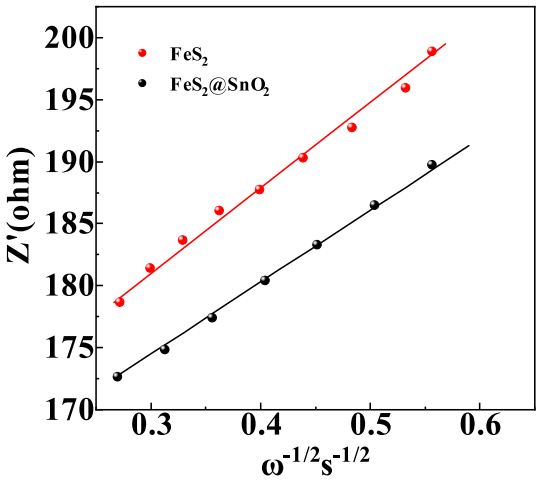

Fig. 5 The plot demonstrating the correlation between Z_{re} and $\omega^{-1/2}s^{-1/2}$.

experiment can be fitted and analyzed, and the Warburg impedance parameters can be further obtained. The voltage amplitude of the EIS test is 5 mV, and the frequency range is $10^6 \sim 10^3$ Hz. Fig. 4a presents the Nyquist plots of the FeS_2@SnO_2 composite material and the FeS_2 material. Compared with FeS_2, the FeS_2@SnO_2 curve exhibits a smaller decrease in curvature radius, suggesting that the SnO_2 coating significantly enhances the electrical conductivity of FeS_2. Fig. 4b presents the surface morphology of FeS_2@SnO_2 after 100 cycles of electrochemical testing. Due to the formation of SnS_2 and the SEI film during the cycling process, the surface morphology of the composite material has changed after multiple cycles, but no structural collapse has occurred. The Weber impedance can be obtained by calculating the curvature of the impedance curve fitting (the specific formula is shown as follows), and then the lithium-ion diffusion coefficient in the FeS_2@SnO_2 electrode can be acquired.

$$Z_{re} = \sigma\omega^{-1/2} \tag{5}$$

$$D_{Li^+} = \frac{R^2T^2}{2A^2n^4F^4C^2\sigma^2} \tag{6}$$

By plotting the curve of Z_{re} against $\omega^{-1/2}$ and analyzing the slope of the resulting curve, in conjunction with the aforementioned formula, the Warburg impedance of FeS_2 and FeS_2@SnO_2 can be determined, as illustrated in Fig. 5. The computed diffusion coefficients of lithium ions in FeS_2 and FeS_2@SnO_2 electrodes are 5.815×10^{-18} cm^2/s and 8.304×10^{-18} cm^2/s (as shown in Table 1), confirming that the FeS_2 composite exhibits superior conductivity and lithium-ion diffusion efficiency.

The results demonstrate that doping and encapsulation of SnO_2 promote lithium-ion transport and serve as effective strategies for enhancing the electrode's high-rate capability and charge transfer kinetics.

CONCLUSION

In summary, FeS_2@SnO_2 composite materials with a polymer-encapsulated structure were successfully synthesized via a combination of hydrothermal and ultrasonic-assisted solvothermal methods. This material is proposed as a novel anode candidate for LIBs. The structural and morphological features of the FeS_2@SnO_2 composite were analyzed using SEM, XPS, TEM, and XRD. Electrochemical investigations demonstrated that the incorporation of SnO_2 between FeS_2 nanoparticles significantly enhances the structural stability of FeS_2, suppresses electrode swelling during delithiation, and improves both capacity retention and coulombic efficiency. Experimental results revealed that the FeS_2@SnO_2 composite exhibits superior cycling stability and enhanced lithium-ion diffusion ki-

netics compared to FeS_2 nanoparticles. The composite demonstrated 487.8 mAh/g capacity retention after 100 cycles at 0.1 A/g. These findings suggest that the FeS_2@SnO_2 composite possesses excellent electrochemical performance and holds great promise for application in next-generation high-performance LIBs.

REFERENCES

1. Shiwen Z, Taoming Y, Zhuoran S, Wenjing S, Lili L, Shujun D (2024) Multilayer coated SiO_2@NC@TiN carbon nanofibers as anode with exceptional cycling stability. *J Solid State Electrochem* **29**, 1–10.
2. Junzhe L, Chao W, Rui W, Chaofeng Z, Guanjie L, Kenneth D, Shilin Z, Zaiping G (2024) Progress and perspectives on iron-based electrode materials for alkali metal-ion batteries: a critical review. *Chem Soc Rev* **53**, 4154–4229.
3. Xin L, Chenglong S, Xinlu W, Jinjin W, Guixia L, Wensheng Y, Xiangting D, Jinxian W (2022) Preparation of Fe_3O_4/FexSy heterostructures via electrochemical deposition method and their enhanced electrochemical performance for lithium-sulfur batteries. *Chem Eng J* **446**, 137267.
4. Yongping G, Feiqiang X, Jianmin L, Huadong Y, Chengbin J, Liyuan Z, Cong F, Ouwei S, et al (2016) One-pot biotemplate synthesis of FeS_2 decorated sulfur-doped carbon fiber as high capacity anode for lithium-ion batteries. *Electrochim Acta* **209**, 201–209.
5. Qianting X, Huaiguo X, Shengping G (2018) FeS_2 walnut-like microspheres wrapped with rGO as anode material for high-capacity and long-cycle lithium-ion batteries. *Electrochim Acta* **292**, 1–9.
6. Ying L, Xue Z, Ping C, Xinrong C, Dongxuan L, Ruiqi W (2023) Properties of hollow yolk-shell NiS_2/FeS_2@NC@NiFe LDH/FeO(OH) nanoflower microspheres as anode materials for lithium-ion batteries. *J Electroanal Chem* **943**, 117606.
7. Dong Z, Guojian W, Jiayuan X, Jun J, Yubin C, Guoliang L (2013) Synthesis and electrochemical performance of bud-like FeS_2 microspheres as anode materials for rechargeable lithium batteries. *Mater Sci Eng B Adv Funct Solid State Mater* **178**, 483–488.
8. Changjian H, Xiaochun L, Jie Z, Bohejin T, Yichuan R (2022) A variety of carbon-coated FeS_2 anodes: FeS_2@CNT with excellent lithium-ion storage performance. *Colloid Surf A Physicochem Eng Asp* **637**, 128226.
9. Yuchen H, Lijie C (2023) SnO_2-coated SiO_2@C core-double-shell nanospheres as high-performance anode materials for lithium-ion batteries. *J Solid State Electrochem* **28**, 2377–2383.
10. Dongxian Z, Yongjin M, Jiayuan X, Xinhui X, Yongquan Q, Jiangping T (2012) FeS_2/C composite as an anode for lithium ion batteries with enhanced reversible capacity. *J Power Sources* **217**, 229–235.
11. Jianpeng C, Deping X, Wenqin J, Wenbin Y, Peng S, Zuyong F, Miao H (2024) SnO_2-MoO_2 nanoparticles coated on graphene oxide as a high-capacity, high-speed, long-life lithium-ion battery anode. *Chem Phys Lett* **835**, 140994.
12. Luying L, Xiaoxiao L, Xuan L, Zhao X, Kefan S, Yunhui Z (2024) Engineering high-performance oxide anodes for lithium storage: SnO_2/TiO_2 heterojunction nanofibers with core-shell structures. *J Electroanal Chem* **968**, 118497.
13. Yujin W, Gao T, Lei S, Yingyi Z, Yongheng Z, Yushan T, Liqun B, Qiuyue L, et al (2023) SnO_2 coated carbon nanospheres: Facile preparation and electrochemical performances as anode materials for lithium ion batteries. *Int J Electrochem Sci* **18**, 100046.
14. Minkang W, Zongzhi T, Xiaojia H, Bin Z, Xinglong Z, Tianhao L, Hui T, Zhaohuan W, et al (2022) *In-situ* synthesized carbon-coated $SnSnO_2$ nanoparticles embedded in carbon nanotubes on Cu foam as anode material for lithium-ion batteries. *J Phys Chem Solids*, 110693.
15. Yanlong T, Yingming X, Xiaoli C, Shan G, Xianfa Z, Hui Z, Lihua H (2022) Lonicerae flos-derived N, S co-doped graphitized carbon uniformly embedded with FeS_2 nanoparticles as anode materials for high performance lithium ion batteries. *J Alloy Compd* **909**, 164707.
16. Qianting X, Jiachuang L, Huaiguo X, Shengping G (2018) Effective combination of FeS_2 microspheres and Fe_3S_4 microcubes with rGO as anode material for high-capacity and long-cycle lithium-ion batteries. *J Power Sources* **396**, 675–682.
17. Beining Z, Chen C, Xinke H, Tao W, Cuiping G, Sang Woo J, Jiarui H (2024) Polyaniline-coated flower-like iron oxide served as anode material for superior-performance lithium-ion batteries. *J Electroanal Chem* **967**, 118484.
18. Lixuan Z, Fan P, Man Z, Dan L, Qichang P, Guanhua Y, Fenghua Z, Youguo H, et al (2022) Heterostructured FeS_2/SnS_2 nanoparticles anchored on graphene for advanced lithium and sodium-ion batteries. *Appl Surf Sci* **606**, 154864.
19. Azam Mohd A, Safie Nur E, Ahmad Aina S, Yuza Nor A, Zulkifli Nor Syazana A (2021) Recent advances of silicon, carbon composites and tin oxide as new anode materials for lithium-ion battery: A comprehensive review. *J Energy Storage* **33**, 102096.
20. Peng J, Qiong W, Boya W, Xu G, Yun Z, Hao W (2020) Encapsulating yolk-shell FeS_2@carbon microboxes into interconnected graphene framework for ultrafast lithium/sodium storage. *J Carbon* **159**, 366–377.
21. Guosong L, Bin C, Zhenyu H, Hao G, Jingwei Z, Ruixiang X, Ying L, Jing X, et al (2024) Fe_2O_3@$FeSe_2$ heterostructure as high-performance supercapacitor negative electrode material. *J Energy Storage* **88**, 111544.
22. Fangwei X, Chunjie X, Yazhou L, Zuzhi T, Chao M, Shu X, Zhibao L, Zia Ur R, et al (2023) Cubic FeS_2 enabling robust polysulfide adsorption and catalysis in lithium/sulfur batteries. *J Energy Storage* **72**, 108712.
23. Alireza H, Mohammadreza Y, Zeinab S (2025) N-doped SnO_2 Nanowire@Void@N-doped carbon as binder free lithium ion battery anode, with high capacity and superior capacity retention. *J Alloys Compd* **1033**, 181202.